Nucleic Acids Research, 2023 **1**
https://doi.org/10.1093/nar/gkad106

Linker histone H1 modulates defense priming and immunity in plants

Arsheed H. Sheikh[1,*], Kashif Nawaz[1], Naheed Tabassum[1], Marilia Almeida-Trapp[1], Kiruthiga G. Mariappan[1], Hanna Alhoraibi[2], Naganand Rayapuram[1], Manuel Aranda[1], Martin Groth[3] and Heribert Hirt[1,*]

[1]King Abdullah University of Science and Technology, KAUST, 23955 Thuwal, Saudi Arabia, [2]Department of Biochemistry, Faculty of Science, King Abdulaziz University, 21551 Jeddah, Saudi Arabia and [3]Institute of Functional Epigenetics, Helmholtz Munich, 85764 Neuherberg, Germany

Received April 20, 2022; Revised January 17, 2023; Editorial Decision February 04, 2023; Accepted February 07, 2023

ABSTRACT

Linker H1 histones play an important role in animal and human pathogenesis, but their function in plant immunity is poorly understood. Here, we analyzed mutants of the three canonical variants of Arabidopsis H1 histones, namely H1.1, H1.2 and H1.3. We observed that double *h1.1h1.2* and triple *h1.1h1.2h1.3* (*3h1*) mutants were resistant to *Pseudomonas syringae* and *Botrytis cinerea* infections. Transcriptome analysis of *3h1* mutant plants showed H1s play a key role in regulating the expression of early and late defense genes upon pathogen challenge. Moreover, *3h1* mutant plants showed enhanced production of reactive oxygen species and activation of mitogen activated protein kinases upon pathogen-associated molecular pattern (PAMP) treatment. However, *3h1* mutant plants were insensitive to priming with flg22, a well-known bacterial PAMP which induces enhanced resistance in WT plants. The defective defense response in *3h1* upon priming was correlated with altered DNA methylation and reduced global H3K56ac levels. Our data place H1 as a molecular gatekeeper in governing dynamic changes in the chromatin landscape of defense genes during plant pathogen interaction.

INTRODUCTION

Plants face constant changes in their homeostasis, so they have evolved complex mechanisms to deal with external abiotic and biotic stresses. Plants can sense microbes by membrane-localized pattern recognition receptors (PRRs) of conserved pathogen/microbe-associated molecular patterns (PAMPs/MAMPs), thereby triggering PAMP/MAMP triggered immunity (PTI/MTI) (1). After recognition, downstream signaling responses are triggered, which include production of reactive oxygen species (ROS), activation of mitogen-activated protein kinases (MAPKs), and activation of defense genes (2). PTI also changes the plant defense hormone profiles (like salicylic acid and jasmonic acid) to optimize the immune response toward pathogens (3). Successful pathogens deliver effector proteins into the plant cells to overcome PTI, causing disease in susceptible plants called effector-triggered susceptibility (ETS). However, resistant plants recognize effectors via intracellular nucleotide-binding domain leucine-rich repeat (NLR) receptors to mount effector triggered immunity (ETI) (4).

In plants, a previous stressful experience modulates the cellular machinery to confer a robust response upon a recurring stress; a phenomenon called priming (5). Priming of plants can efficiently increase the tolerance and survival of plants to different stresses. One of the well-characterized PAMPs is a 22-amino-acid long epitope of *Pseudomonas* flagellin (flg22), which is recognized by the FLS2 receptor (6). Pretreatment with flg22 induces defense priming in Arabidopsis enhancing plant resistance to subsequent challenge with pathogenic *Pseudomonas syringae* (7).

The execution of early and late immune responses upon pathogen recognition is fundamentally modulated by optimal gene expression (8,9). Chromatin changes and nucleosome dynamics fine-tune gene expression in stress conditions. Besides core nucleosomal histones, linker histones are major constituents of eukaryotic chromatin (10). In eukaryotes, linker histone H1 has a conserved tripartite structure consisting of (i) a short and flexible N-terminal tail, (ii) a dyad binding central globular domain (GH1) and (iii) a structurally disordered lysine-rich C-terminal tail (11). Linker histone H1 binds to the nucleosome to facilitate chromatin folding usually into higher order structures (12). In addition to regulating basic biological processes like DNA replication, chromosome segregation, and DNA

*To whom correspondence should be addressed. Tel: +966128082959; Email: heribert.hirt@kaust.edu.sa
Correspondence may also be addressed to Arsheed H. Sheikh. Tel: +966565674649; Email: arsheed.sheikh@kaust.edu.sa

repair, H1 regulates gene expression by modulating RNA polymerase II accessibility to chromatin (12–14).

H1 deposition is part of the crosstalk with the epigenetic landscape, notably DNA methylation and histone H3 methylation (15–17). H1 mutants are difficult to study owing to the high functional redundancy between H1 variants. Deletion of H1 in mouse and Drosophila is lethal but not in other organisms like Tetrahymena, yeast, fungi and worms (12,18). Arabidopsis has three canonical variants of H1 namely, H1.1, H1.2 and stress-regulated H1.3 (19). Interestingly, the mutants are viable with morphological and developmental defects (17). In Arabidopsis root and shoot tissues, H1.1 and H1.2 are ubiquitously expressed during vegetative development. At the genome level, H1 is distributed in heterochromatin and euchromatin showing enrichment at 3′ and 5′ ends of transposable elements (TEs). Over gene bodies, H1 presence is usually anticorrelated to transcription and H3K4me3 levels (19,20). All DNA methylation patterns in Arabidopsis (i.e. CG, CHG, CHH), are regulated by H1 mainly in heterochromatin but also in euchromatin (21,22). H1 possibly creates a structural barrier that restricts RNA-dependent DNA methylation to euchromatic regions and requires DDM1-mediated accessibility to DNA methyltransferases MET1, CMT1 and CMT2 for maintenance of heterochromatic DNA methylation (21,23).

In this study, we demonstrate that Arabidopsis H1 knockout mutants have elevated basal immune levels and are resistant against a bacterial and a fungal pathogen. However, *3h1* mutant plants are compromised in flg22 triggered priming. The altered DNA methylation and reduced H3K56ac profiles in *3h1* after flg22-treatment provide strong evidence of the molecular mechanism of the priming deficient phenotype of *3h1* mutant.

MATERIALS AND METHODS

Plant material and growth conditions

The experiments were performed by using Arabidopsis (*Arabidopsis thaliana*) lines in the Col-0 ecotype background unless stated otherwise. *h1.1* (SALK_N628430) and *h1.2* (GK-116E080) mutants were obtained from the European Arabidopsis Stock Center. *h1.3* (GT18298) in the L*er* background was obtained from the Cold Spring Harbor Laboratory collection. The *h1.1h1.2h1.3* (*3h1*) triple mutant was obtained by crossing *h1.1h1.2* with *h1.3* (17). Plants were grown on soil (jiffy pots, http://www.jiffypot.com/), in plant growth chambers (Percival Scientific) under short-day conditions (8 h light/ 16 h dark) at 22°C.

Pathogen infection assays

P. syringae tomato pv. DC3000 (*Pst* DC3000) strain was grown on King B agar plates with 50 μg/ml rifampicin at 28°C. Bacteria were adjusted to 10^6 cfu/ml in 10 mM $MgCl_2$ and inoculated to four-week-old plants by either syringe or spray infection. Bacteria were released from three leaf discs (4mm) in 500 μl of 10 mM $MgCl_2$ with 0.01% Silwet 77 by incubating at 28°C at 1000 rpm for 1 h. Serial dilutions were plated on LB medium with appropriated antibiotic. After incubation at 28°C, bacterial colonies were counted. The experiment was repeated three times with similar results.

Botrytis cinerea infection was performed as previously described (24). Briefly, 4-week-old plants were inoculated with *Botrytis cinerea* (strain: B05.10) by placing a 5 μl droplet of a spore suspension (5×10^5 spores/ml) on each rosette leaf (three fully expanded leaves per plant). Trays were covered by a transparent plastic lid to maintain high humidity. Lesion diameter was measured after 2 days of infection using ImageJ analysis tool.

ROS burst assays

ROS burst was determined by the luminol-based assay described before with modifications (25). Leaf discs were incubated overnight in a white 96-well plate in water to reduce the wounding effect. Next day, the water was replaced by 100 μl of reaction solution containing 50 μM of luminol (Sigma) and 10 μg/ml of horseradish peroxidase (Sigma) supplemented with 1 μM of flg22. The measurement was conducted immediately with a luminometer (GloMax, Promega) for a period of 40 min with a 1 min reading interval between readings. The measurements are shown as means of RLU (relative light units). The experiments were repeated three times with similar results.

MAPK activation assays

Adult plants or seedlings treated with 1 μM of flg22 were harvested at the indicated time points. Proteins were extracted using extraction buffer. The frozen seedlings were homogenized in 100 μL of extraction buffer (150 mM Tris–HCl, pH 7.5, 150 mM NaCl, 5 mM EDTA, 2 mM EGTA, 5% glycerol, 10 mM DTT and 1× Pierce Protease and Phosphatase tablet (thermo#A32959)). Twenty micrograms of protein were separated on a 10% polyacrylamide gel and transferred on a PVDF membrane. After overnight blocking with TBST–5% milk, the membrane was washed 3 times with TBST. Immunoblot analysis was performed using anti-phospho-p44/42 MAPK (1:5000; Cell Signaling Technology) for 2 h as primary antibody and peroxidase-conjugated goat anti-rabbit antibody (1:10 000; Promega) for 1 h with 5 times 10 min washes in-between the incubations. The experiment was repeated twice with similar results.

Hormone measurements

The extraction of phytohormones and camalexin was performed as described (26). The compounds were quantified by HPLC-ESI-SRM in a Thermo Fisher TQS-Altis Triple Quadrupole Mass Spectrometer coupled to a Thermo Scientific Vanquish MD HPLC system. The chromatographic separation was carried out in a UPLC column (Agilent Eclipse Plus C18, RRHD, 1.8 um, 2.1 × 50 mm), and the compounds were eluted using water (A) and acetonitrile (B) as mobile phase at 0.6 mL/min and in a gradient elution mode as following: 10% B for 0.5 min, 10–55% of B at 4.5 min, 55–100% B at 4.7 min, 100% until 6.0 min, 100–10% B at 6.1% and 10% until 8 min. The column was kept at 55°C. The statistical significance from three replicates was evaluated by ANOVA followed by Tukey Test (Tukey HSD).

Callose deposition

Callose deposition was conducted as described by Wang *et al.* (27) with modifications. Briefly, 10-day-old WT and *3h1* mutant plants were treated with 1 μM of flg22. After 24 h, seedlings from each genotype were destained in ethanol:acetic acid solution (3:1) for 3–4 h. Samples were washed with 150 mM K_2HPO_4 for 30 min. Cleared leaves were stained with 0.01% aniline blue (Sigma) in 150 mM K_2HPO_4 (pH 9.5) overnight in dark with constant shaking. Callose deposits were visualized under a DAPI filter using a fluorescence microscope. Callose deposits were counted using ImageJ software.

RNA extraction and real-time RT-PCR analysis

Total RNAs were extracted from 4-week-old adult plants using NucleoSpin RNA Plant (MACHEREY-NAGEL) kit, according to the manufacturer's instructions. First strand cDNA was synthesized from 1μg of total RNAs using SuperScript First-Strand Synthesis System for RT-PCR according to the manual instructions. Then 2 μl of 10 times diluted cDNA was used for CFX96 Touch Real-Time PCR Detection System (Bio-Rad) for Syber green based quantitative PCR analysis. The specificity of amplification products was determined by melting curves. Tubulin was used as internal control for signal normalization. The relative expression level of the selected genes was calculated based on ΔΔCt method. The primers used are listed in Supplementary Table S2.

RNA sequencing and analysis

RNA-seq was performed from mRNA libraries with 1μg of total plant RNA using TrueSeq standard mRNA Library Prep kit (Illumina). Pooled libraries were sequenced using Illumina HiSeq 4000 platform. RNA-seq generated 1538 million raw read pairs from 36 libraries (including three time points; 0, 6 and 24 h in methylation data). Adapters, primers, and low-quality bases were removed from the ends of raw reads using Trimmomatic v0.38 (28). The resulting trimmed reads were mapped to the TAIR10 genome using Tophat2 v2.1.1 (29). Read counts were generated for all samples from corresponding bam files using BEDTools v2.29.0 (30). DESeq2 (31) was run with read counts to identify DEGs between several conditions (comparison description: refer to RNA-seq excel file) with FDR ≤0.01. All the heatmaps generated for RNA-seq were plotted using the R package pheatmap (https://cran.r-project.org/web/packages/pheatmap/index.html). Clustering of genes based on their expression within conditions was performed in basic R language using hierarchical and *k* -means clustering. Functional enrichment of DEGs was carried out with AgriGO (32) using default settings. GO terms with $P \leq 0.05$ were considered significant, and the occurrence of at least five times in the background set was additionally required for DEGs.

Whole genome bisulfite sequencing and analysis

DNAs from plant samples were extracted by NucleoSpin Plant II kit from Macherey-Nagel. DNA samples were processed by Zymo Research (USA) for WGBS using Methyl-MaxiSeq® Library Preparation procedure. Briefly, 250 ng of starting input genomic DNA was digested with 1 unit of Zymo Research dsDNA ShearaseTM Plus (Cat#: E2018-50). The fragments produced were end-blunted and 3'-terminal-A extended, then purified using DNA Clean & ConcentratorTM-5 (Cat#: D4003). The A-tailed fragments were ligated to pre-annealed adapters containing 5'-methyl-cytosine instead of cytosine according to Illumina's specified guidelines. Adaptor-ligated fragments ≥ 50 bp in size were recovered using the DNA Clean & ConcentratorTM-5 (Cat#: D4003). The fragments were then bisulfite-treated using the EZ DNA Methylation-LightningTM Kit (Cat#: D5030). PCR was performed with Illumina indices and the resulting products were purified with DNA Clean & ConcentratorTM-5 (Cat#: D4003). Size and concentration of the fragments were confirmed on the Agilent 2200 TapeStation. Libraries were sequenced on an Illumina NovaSeq instrument.

The analysis of WGBS was performed as described by Cokus *et al.* (33). Briefly, sequencing of the 12 libraries (4 conditions, 3 biological replicates each) resulted in 991 million read pairs. Adapters were trimmed from the raw sequences using Trimmomatic v0.38. Subsequently, trimmed reads were mapped to the TAIR10 genome using Bowtie2 v2.2.5 (34), and methylation calls were performed using Bismark v0.22.3 (35). Four filters were used to reduce false positives. First, we removed the reads with three or more consecutive CHH methylations as described earlier (33). Second, with k methylated reads mapping, the probability of it occurring through sequencing error (that is, unmethylated position appearing as methylated) was modeled using a binomial distribution $B(n, p)$, where n is the coverage (methylated + unmethylated reads) and p is the probability of sequencing error (set to 0.01). We kept positions with k methylated reads if $P(X \geq k) < 0.05$ (post-FDR correction). Third, retained methylated positions had to have ≥1 methylated read in all three biological replicates of at least one growth condition. Finally, the median coverage of retained positions across all 12 samples had to be ≥10. After calling significant methylation in each replicate separately, we merged the replicates from the corresponding condition by taking the mean for each methylation context. This yields a final average bedgraph file for each of the four conditions which have been used for further analyses. All the average line plots of methylation around and within the genes have been plotted by deepTools (36). All boxplots for methylation have been generated using the R package ggplot2. The snapshots used in the analyses were taken from the integrated genome browser IGB v9.8.1.

Assignment of genomic context to methylated cytosines

On the basis of the gene annotation of the TAIR10 (GFF3 file) and the positional coordinates of the methylated cytosines produced by Bismark, we annotated every methylated cytosine based on the genomic context using bedtools intersect, which is a common genome analysis toolkit. Based on the GFF3 file we included whether the methylated position resides in a genic or intergenic region, and

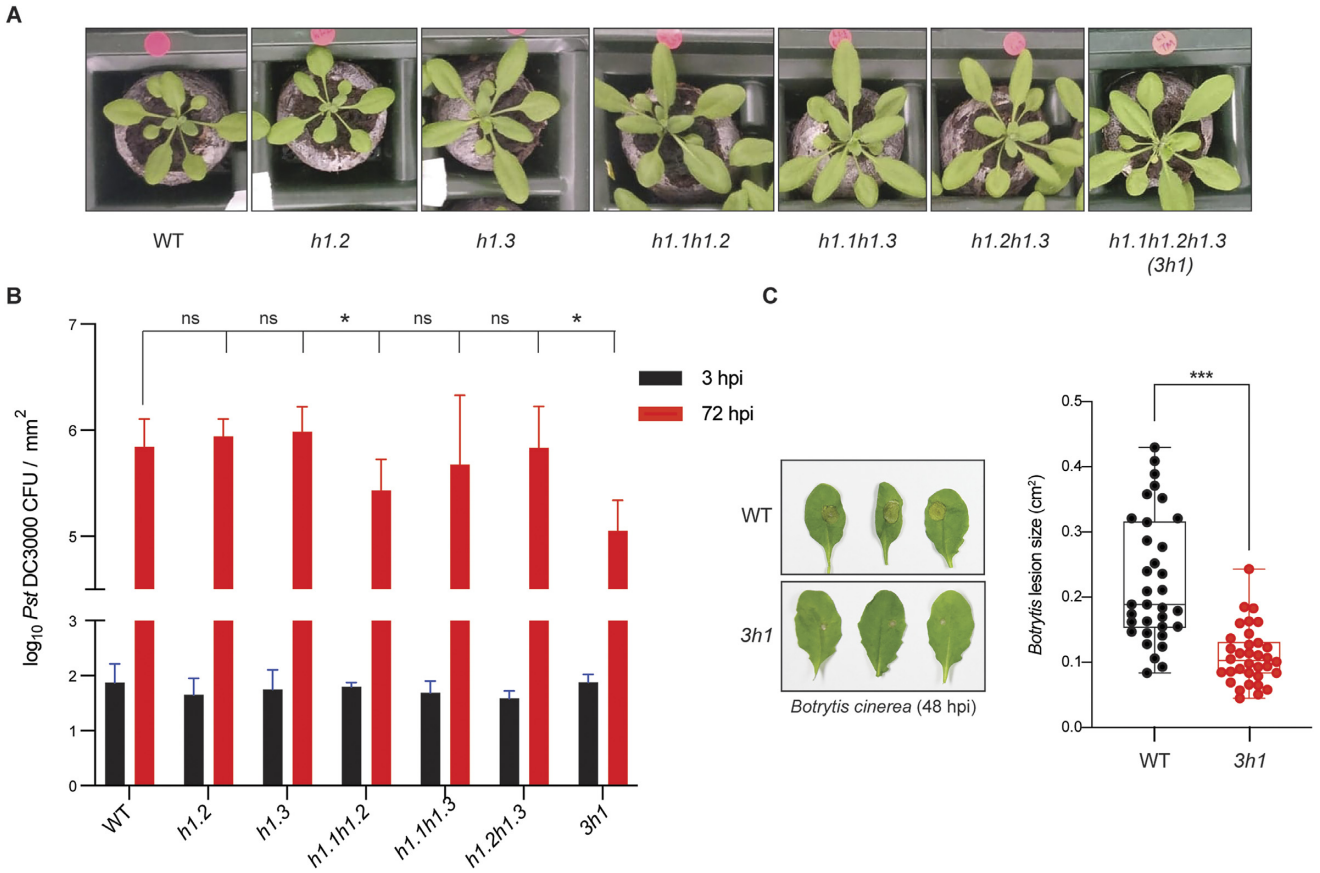

Figure 1. Linker histone mutant *3h1* is resistant to pathogen infection. (**A**) Morphology of 4-week-old wild-type (WT), single (*h1.2*, *h1.3*), double (*h1.1h1.2*, *h1.1h1.3*, *h1.2h1.3*) and triple (*h1.1h1.2h1.3* or *3h1*) mutants of Arabidopsis H1 grown on pots. (**B**) Quantification of bacterial colonies in different *h1* mutants after spray inoculation with *Pseudomonas syringae* pv DC3000 (*Pst* DC3000) at 3 and 72 hours post infection (hpi). (**C**) Quantification of fungal infection as reflected by the lesion size in the WT and *3h1* after 48 h of *Botrytis cinerea* drop inoculation on 4-week-old plants. The data is represented as mean ± SEM where * and *** indicate $P < 0.05$ and 0.001 compared to WT, as determined by ANOVA significance test.

the distances to the 5′ and 3′ ends of each genomic feature (gene/intergenic region/exon/intron).

PCA and correlation matrices

Median methylation levels of methylated genes and $\log_2$FPKM of expressed genes were shifted to be zero-centered and analyzed by PCA using the prcomp function in R. Using the same data, we calculated correlation matrices (Pearson correlation coefficient) and clustered samples with hclust implemented in R using complete linkage and Euclidean distance.

Western blotting of histones

Nuclei were isolated from ground powder as already described (37). 5× SDS Loading dye was directly added to the nuclei and boiled at 85°C for 10 min and later loaded on 15% SDS-PAGE gel. Later, western blotting was performed as described in MAPK activation assays section.

DNaseI accessibility PCR

DNaseI (Promega) treatment was given to isolated nuclei for 5 min at 37°C and reaction was stopped by adding EDTA to the tubes. Later DNA was isolated from the samples and accessibility PCR assay performed as already described (38).

RESULTS

Linker histone H1 regulates plant immunity against pathogen infection

In an effort to understand the role of linker histone proteins in plant immunity, we analyzed Arabidopsis H1 mutants for developmental and pathogen phenotypes. The H1 mutants used in the study were either knockouts of single, double or all three isoforms of H1. Interestingly, all H1 mutants were viable and grew well with no visible morphological defects in pots (Figure 1A). We tested 4-week-old single mutants (*h1.2* and *h1.3*), double mutants (*h1.1h1.2*, *h1.1h1.3* and *h1.2h1.3*) and the triple mutant *h1.1h1.2h1.3* (called *3h1* from now onwards) against virulent *Pseudomonas syringae* pv. *tomato* DC3000 (*Pst* DC3000). We observed that *h1.1h1.2* and *3h1* are significantly resistant to *Pst* DC3000 infection while single *h1s*, double *h.1.1h1.3* and *h1.2h1.3* mutants allow proliferation of *Pst* DC3000 to a similar extent as found in wild type (WT) plants (Figure 1B). These observations suggest that two main isoforms H1.1 and H1.2

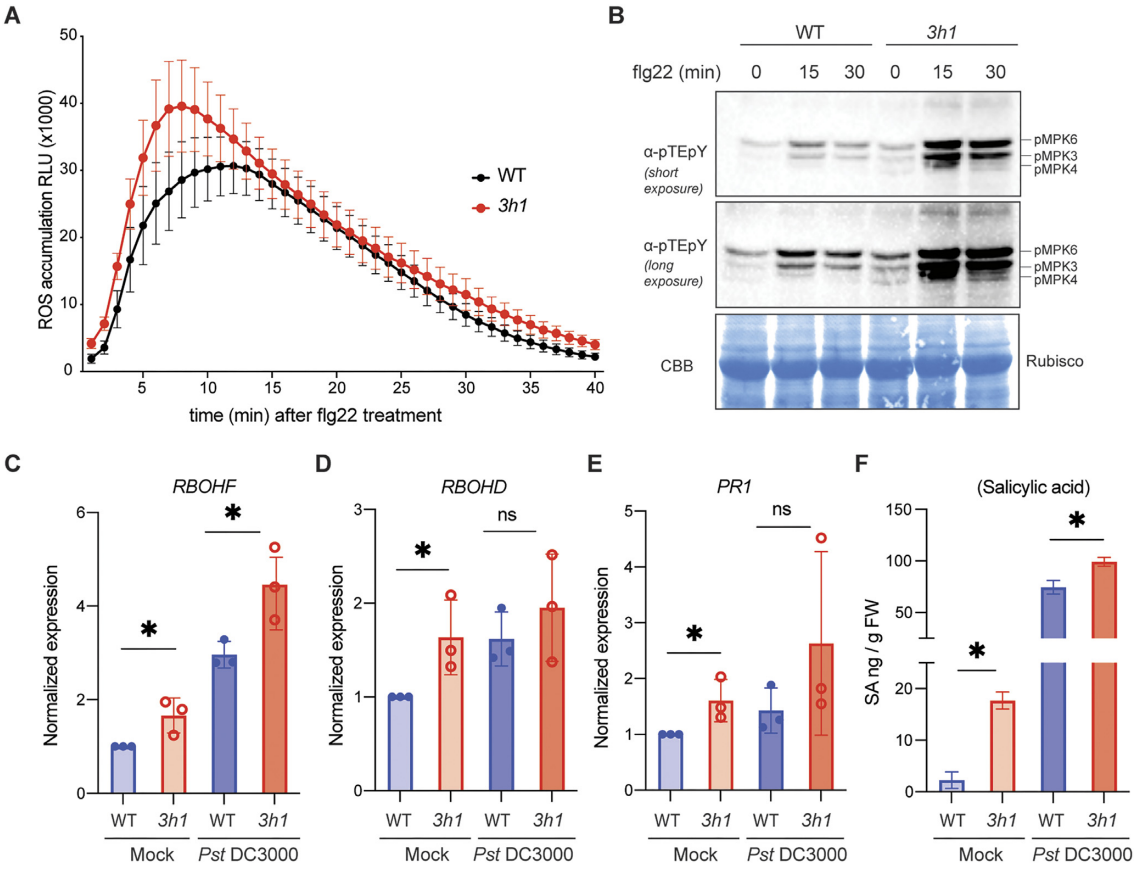

Figure 2. *3h1* mutant shows elevated innate immunity levels. (**A**) Reactive oxygen species (ROS) levels quantified over 40 min in WT and *3h1* leaf discs triggered by 1 μM flg22 treatment. (**B**) MAPK activation monitored with anti-pTEpY antibody indicating phosphorylation of MPK6, MPK3 and MPK4 in WT and *3h1* plants after 1 μM flg22 treatment for 15 and 30 min. CBB stain of Rubisco serves as a loading control. (**C–E**) Expression of key innate immunity genes *RBOHD*, *RBOHF* and *PR1* after 6h of mock treatment or *Pst* DC3000 infection. (**F**) Salicylic acid (SA) quantification in WT and *3h1* plants is shown as ng/g of fresh weight. The data are shown as means ± SEMs from three replicates. Asterisk indicates a significant difference with $P < 0.05$.

together are important in modulating plant immunity. As *3h1* showed the strongest resistance phenotype, we carried out the rest of the analysis using the triple *3h1* mutant. When challenged with the fungal pathogen *Botrytis cinerea*, *3h1* plants efficiently restricted fungal infection compared with WT plants as depicted by the smaller lesion size (Figure 1C).

3h1 mutant plants have elevated basal immune responses

To examine the effect of the loss of linker histones on basal immune responses, we performed a number of flg22-induced early and late PTI readouts in *3h1* mutant as compared to WT plants. For early PTI events, *3h1* plants produced higher levels of reactive oxygen species (ROS) than WT plants upon flg22 or chitin treatment (Figure 2A and Supplementary Figure S1A). We also observed an elevated activation of the mitogen-activated protein kinases MPK3, 4 and 6 in *3h1* mutant as compared to WT after 15 and 30 min of flg22 elicitation in both adult plants and seedlings (Figure 2B and Supplementary Figure S1B). The key plant enzymes producing ROS in responses to pathogen defense are RBOHD and RBOHF (39). We observed a higher level of both *RBOHD* and *RBOHF* levels in *Pst* DC3000 treated *3h1* plants (Figure 2C,D). Also, *PR1* defense gene expression was elevated in *3h1* mutant while a dynamic expression of *FRK1* and *MYB51* was observed before and after *Pst* DC3000 treatment (Figure 2E and Supplementary Figure S1C, D). The defense related hormones salicylic acid (SA) and jasmonic acid (JA) are key to optimize immune outputs, we thus quantified SA and JA in *3h1* mutant plants after pathogen infection. We observed elevated levels of SA in adult *3h1* plants compared to WT when challenged with *Pst* DC3000, while there was a subtle but insignificant increase in JA levels (Figure 2F and Supplementary Figure S1E). Together, these results indicate that a deficiency in linker H1 affects basal immune responses in plants, possibly through H1-mediated regulation of the plant gene expression.

H1 regulates the plant defense gene expression profile

In order to understand the immunity phenotype of the *3h1* mutant, we performed RNA sequencing of adult WT and *3h1* plants after challenge with *Pst* DC3000 for early (6 h) and late (24 h) defense responses (Figure 3A). Principal components analysis (PCA) revealed that biological replicates clustered together (Supplementary Figure S2A), indicating good reproducibility of our experiments. Additionally, the 0 to 24 hpi (hours post infection) samples were separated in the PCA plot, suggesting that gene

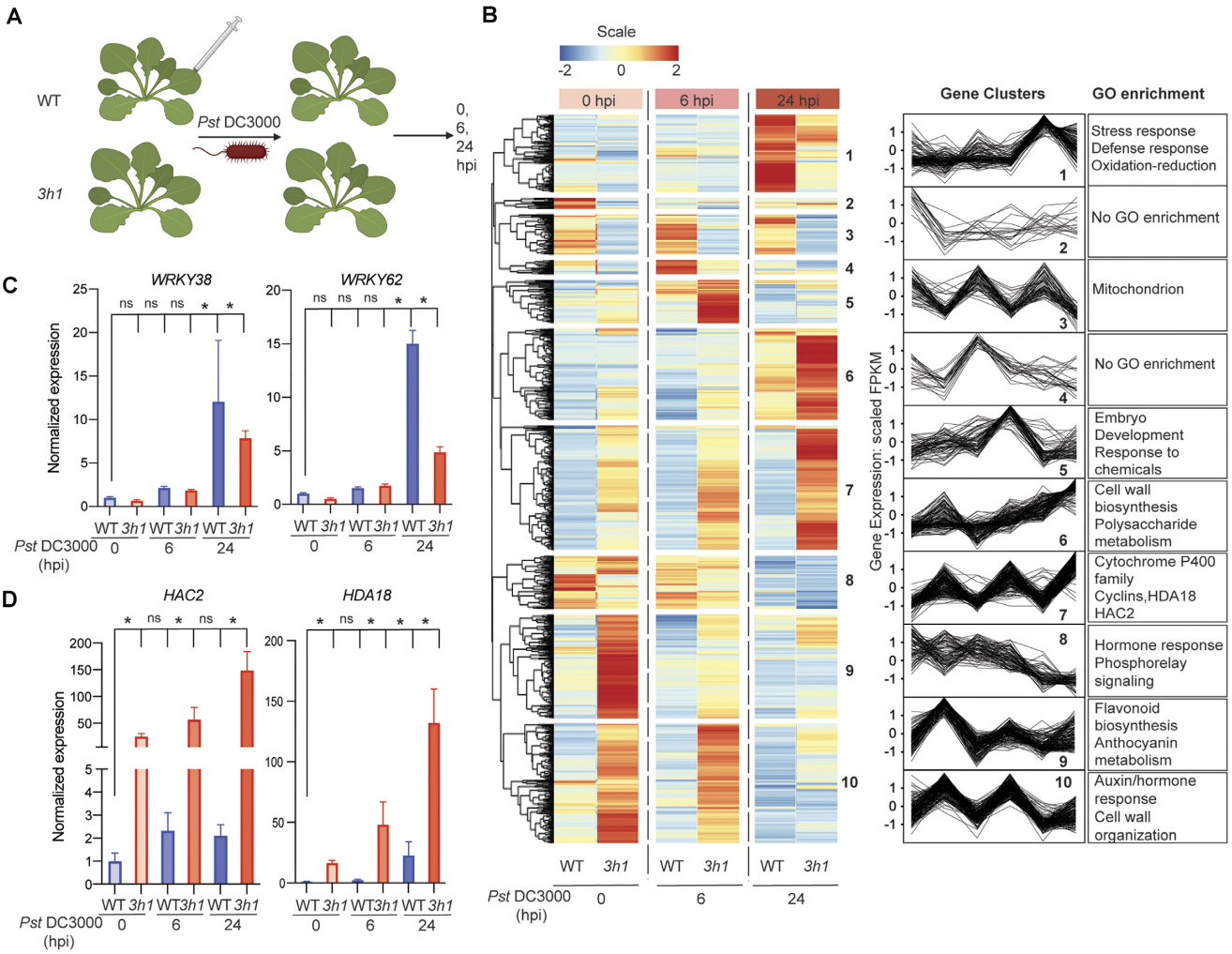

Figure 3. Dynamic transcriptome of *3h1* during pathogen infection. (**A**) Schematic diagram of RNA seq procedure where 4-week-old adult plants were infected with *Pst* DC3000 and samples harvested at 0, 6 and 24 h after infection. (**B**) Hierarchical clustering of *Pst* DC3000-infected (6 and 24 h) WT and *3h1* plants compared to control based on differentially expressed RNA transcripts from mRNA seq using DESeq2 (2.0 FC, FDR $P_{adj} < 0.01$). Transcript fold-change depicted as color scale demonstrates $\log_2$ fold changes compared to mean for each transcript across genotype and condition. GO and pathway enrichment terms are depicted for the gene clusters against the background of all transcripts in the heatmap. (**C**, **D**) qRT-PCR validation of selected genes which showed altered expression pattern between WT and *3h1* before and after infection. The data are shown as means ± SEMs from three replicates. Asterisk indicates a significant difference with $P < 0.05$ from two-way ANOVA.

expression changed massively as disease progressed (Supplementary Figure S2A). Differential gene expression analysis identified more than 1600 genes already affected by the genotype before challenge with *Pst* DC3000 (Supplementary Figure S2B). More than 1000 genes were upregulated, and around 600 genes were downregulated in *3h1* in control conditions (Supplementary Figure S2B). When compared to WT, *3h1* plants displayed significant differences in transcript abundance of 924 (638 up- and 286 downregulated) and 2151 (1145 up- and 1006 downregulated) genes after 6 and 24 h of *Pst* DC3000 infection, respectively (Supplementary Figure S2B). Hierarchical clustering identified ten gene clusters with distinct changes in expression in response to *Pst* DC3000 pathogen in *3h1* mutant plants compared to WT (Figure 3B). Notably, the genes in cluster 1, which were highly upregulated in WT at 24 hpi, were repressed in *3h1* mutant plants. This cluster contained a number of defense related genes, including *WRKY38* and *WRKY62*, which are both negative regulators of immunity (40). We confirmed the behavior of this cluster by qRT-PCR analysis of *WRKY38* and *WRKY62,* which both showed reduced expression in *3h1* post-infection by *Pst* DC3000 (Figure 3C). The transcripts of cluster 5, including immunity-related defensins and cytochrome P450 family proteins, were highly upregulated in *3h1* but not in WT at 6 hpi (Figure 3B). Transcripts of cluster 6 and 7 genes showed highly elevated levels in *3h1* mutant plants at 24 hpi (Figure 3B). Whereas the GO terms of cluster 6 genes were associated with cell wall and polysaccharide metabolism, cluster 7 genes contained a number of chromatin-related proteins, including the histone acetyltransferase HAC2 of the CBP family 2 and the histone deacetylase HDA18 of the RPD3/HDA1 superfamily (Figure 3B). By qRT-PCR, we confirmed that *HDA18* and *HAC2* levels strongly increased in *3h1* after *Pst* DC3000 infection compared to WT plants, eluding to the possible fine-tuning of gene expression

by H1 (Figure 3D). Interestingly, cluster 9 genes, encoding flavonoid and anthocyanin secondary metabolite genes, were downregulated upon pathogen infection in WT but not in *3h1,* which showed elevated levels of these pathways before pathogen challenge. To this end, we studied the levels of some of the key defense related secondary metabolites like Callose and Camalexin (41). We observed significantly higher callose deposition in *3h1* than in WT in control conditions (Supplementary Figure S3A, B). Also, compared to WT, higher camalexin amounts were observed in *3h1* under mock conditions, which further significantly increased after *Pst* DC3000 infection (Supplementary Figure S3C, D). Together, these results suggest that H1 histones contribute in orchestrating both early and late responsive plant defense genes.

flg22 induced defense priming is attenuated in *3h1*

To understand whether H1 plays a role in defense priming, we pretreated WT and *3h1* plants with flg22 for 24 hours before *Pst* DC3000 pathogen infection. Compared to water pre-treatment, flg22 treated WT showed reduced disease symptoms of *Pst* DC3000 infection (Figure 4A, B). In contrast, *3h1* plants were insensitive to flg22-induced priming as shown by the similar bacterial titers in *3h1* mutant plants with and without flg22 pre-treatment (Figure 4A, B). We observed a decrease in callose deposition in *3h1* mutant after 24 h of flg22 treatment, although callose deposition was increased in mock-treated *3h1* mutant plants (Supplementary Figure S3A, B). Also, a reduction in camalexin levels was observed in flg22 treated *3h1* plants as compared to WT before and after *Pst* DC3000 challenge (Supplementary Figure S3C, D). The reshaping of the transcriptome in pathogen-challenged tissues is one of the attributes of defense priming (42). To understand the compromised defense priming phenotype in *3h1*, we performed transcriptome analysis of flg22 pre-treated WT and *3h1* plants challenged with *Pst* DC3000 at early (6 h) and late (24 h) time points (Figure 4C). PCA analysis showed the reliability of our biological replicates, and the Venn diagrams represent the numbers of up and downregulated genes after *Pst* DC3000 infection (Supplementary Figure S2C, D). Cluster 1 is comprised of 154 genes that get strongly upregulated in WT plants during early *Pst* DC3000 (6h) infection while the expression is not altered in *3h1* after infection (Figure 4D). Interestingly, GO term analysis shows strong enrichment of these genes in innate immunity and defense signaling. One of the key innate defense marker genes, *WRKY29* (43), was not induced in flg22-treated *3h1* plants after *Pst* DC3000 infection, suggesting a possible explanation for the compromised defense priming phenotype in *3h1* mutant plants (Figure 4E). We also tested the expression pattern of other defense-related genes like *WRKY31* and *MAPKKK15* in Cluster 1 (Figure 4F, G and Supplementary Figure S4A). Their expression behavior was similar to *WRKY29*, suggesting they might orchestrate the changes in plant defense in a concerted manner.

Another stark difference was observed at *HAC2* and *HDA18* as their expression decreased in *3h1* plants after flg22 priming (Supplementary Figure S4B, C), which is in contrast to their expression in non-primed conditions (Figure 3D). These results suggest that an altered regulation of defense priming might occur at the epigenetic level in *3h1* mutant plants.

3h1 plants exhibit dynamic DNA methylation before and after flg22 treatment

The reshaping of the epigenetic landscape leads to a transiently enhanced local immunity followed by a poorly understood defense priming mechanism (42). One of the key epigenetic modifications regulated by H1 histones is DNA methylation (17,44). To further understand the defective priming in *3h1*, we analyzed genome-wide DNA methylation by whole-genome bisulfite sequencing (WGBS) in WT and *3h1* mutants pre- and post-flg22 treatment. To validate the quality of our sequencing data we analyzed the percentage of non-conversion rate by calculating mean methylation ratios of chloroplast genomes (which lacks DNA methylation) in CG, CHG and CHH contexts and observed $<0.5\%$ non-conversion in all samples, which supports that our data meet the standards of acceptable WGBS (Supplementary Table S1, Supplementary Figure S5A-F). Principal components analysis (PCA) and Pearson correlation analysis showed that the biological replicates clustered together (Supplementary Figure S6A–C, D–F) and individual methylation percentages in biological replicates again indicate good reproducibility of our experiments (Supplementary Figure S6G-I). We observed higher global CG and CHG methylation levels in *3h1* as compared to WT (Supplementary Figure S6J–L). Next, we analyzed the methylation dynamics in CG, CHG and CHH contexts for protein coding genes (PCGs) and transposable element (TE) regions. We further divided the protein coding loci into promoters (2 kb upstream) and gene body. We plotted methylation differences in CG, CHG and CHH contexts from all three individual biological replicates and analyzed the effect of flg22 treatment in Col-0 and *3h1* mutant (Supplementary Figure S7). Interestingly we observed a decrease in promoter methylation in *3h1* in CHG and CHH contexts while a subtle but insignificant increase was observed in CG context (Figure 5A, B, Supplementary Figure S7A). On the other hand, an increase in gene body CHG methylation was observed in *3h1* compared to WT (Figure 5A, B, Supplementary Figure S7B). The DNA methylation in all sequence contexts was strongly increased in *3h1* over the TE regions (Figure 5C, D, Supplementary Figure S7C). Flg22 treatment resulted in a further increase in DNA methylation in CG and CHG wile a slight decrease in CHH contexts in TE regions (Figure 5B, Supplementary Figure S7). However, a decrease in promoter and gene body methylation was observed in flg22 treated *3h1* mutant. This suggests that H1 can influence the flg22 triggered methylation changes in PCGs and TEs (Figure 5A, B, Supplementary Figure S7).

Flg22 triggered differential methylation influences defense gene expression in *3h1* plants

To understand the effects of dynamic PCG methylation on gene expression, we focused on the prominent gene clusters (Cluster 1, Figure 4D) where the gene expression strongly

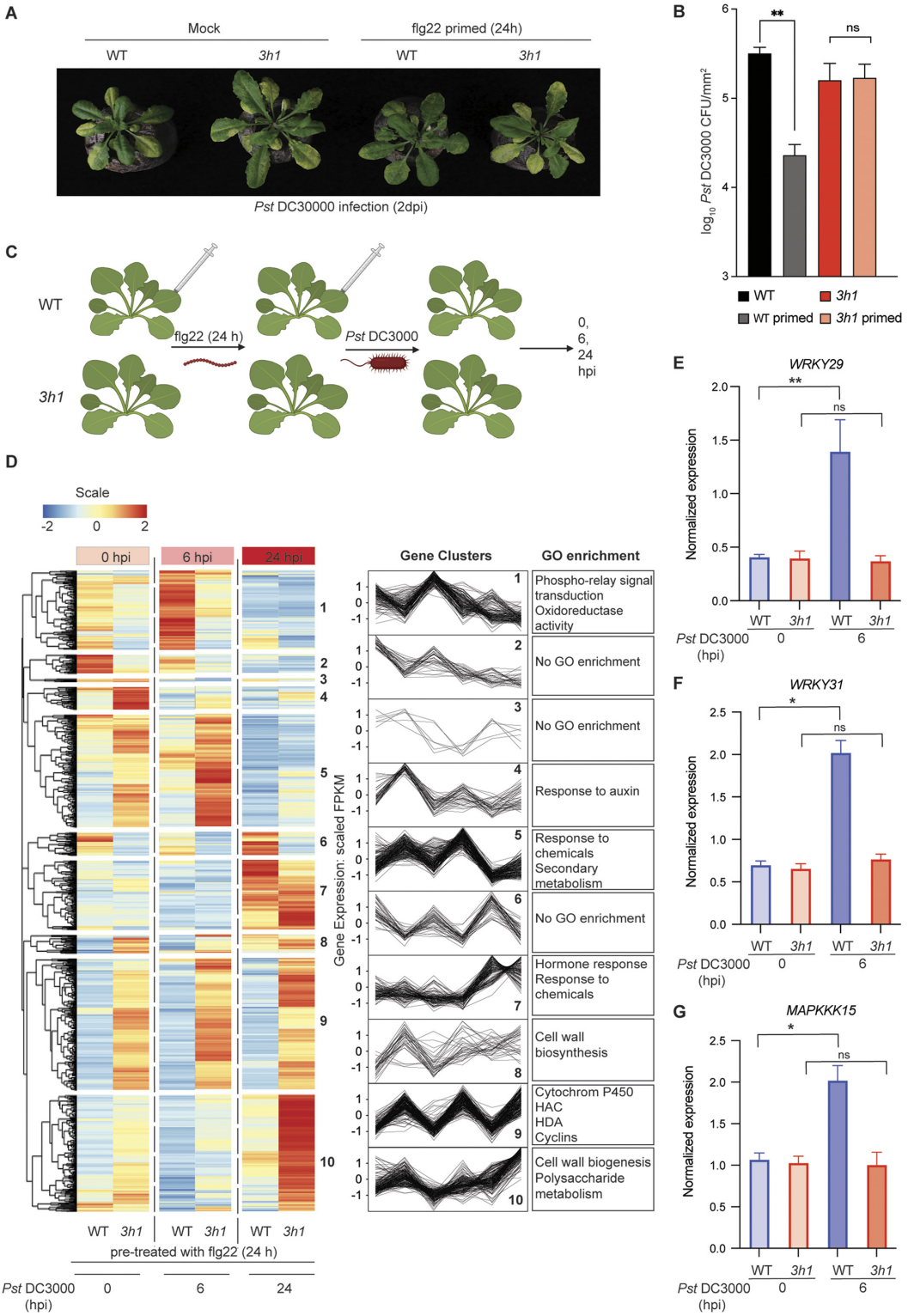

Figure 4. *3h1* is compromised in flg22- triggered defense priming. (**A**) Altered disease symptom development in mock and flg22-treated WT and *3h1* adult plants. Photographs of representative infected plants were taken after 2 days of *Pst* DC3000 infection. (**B**) Bacterial growth of WT and *3h1* plants with and without 24 h of flg22-treatment. (**C**) Schematic diagram of RNA seq where 4-week-old adult plants were first treated with 1 μM flg22 and after 24 h syringe infiltrated with *Pst* DC3000 and samples harvested at 0, 6 and 24 h after infection. (**D**) Heat map showing differentially expressed transcripts of *Pst* DC3000-infected (6 and 24 h) WT and *3h1* plants pre-treated 24 h prior with flg22. Transcript fold-change depicted as color scale demonstrates $\log_2$ fold changes compared to mean for each transcript across genotype and condition (FDR $P_{adj} < 0.01$). GO pathway enrichment terms depicted for the gene clusters against the background of all transcripts in the heatmap. (**E–G**) qRT-PCR validation of *WRKY29*, *WRKY31* and *MAPKKK15* genes which showed altered expression pattern between WT and *3h1* before and after infection when pre-treated with flg22. The data are shown as means ± SEMs from three replicates. Asterisk indicates a significant difference with $P < 0.05$ from multiple comparison two-way ANOVA.

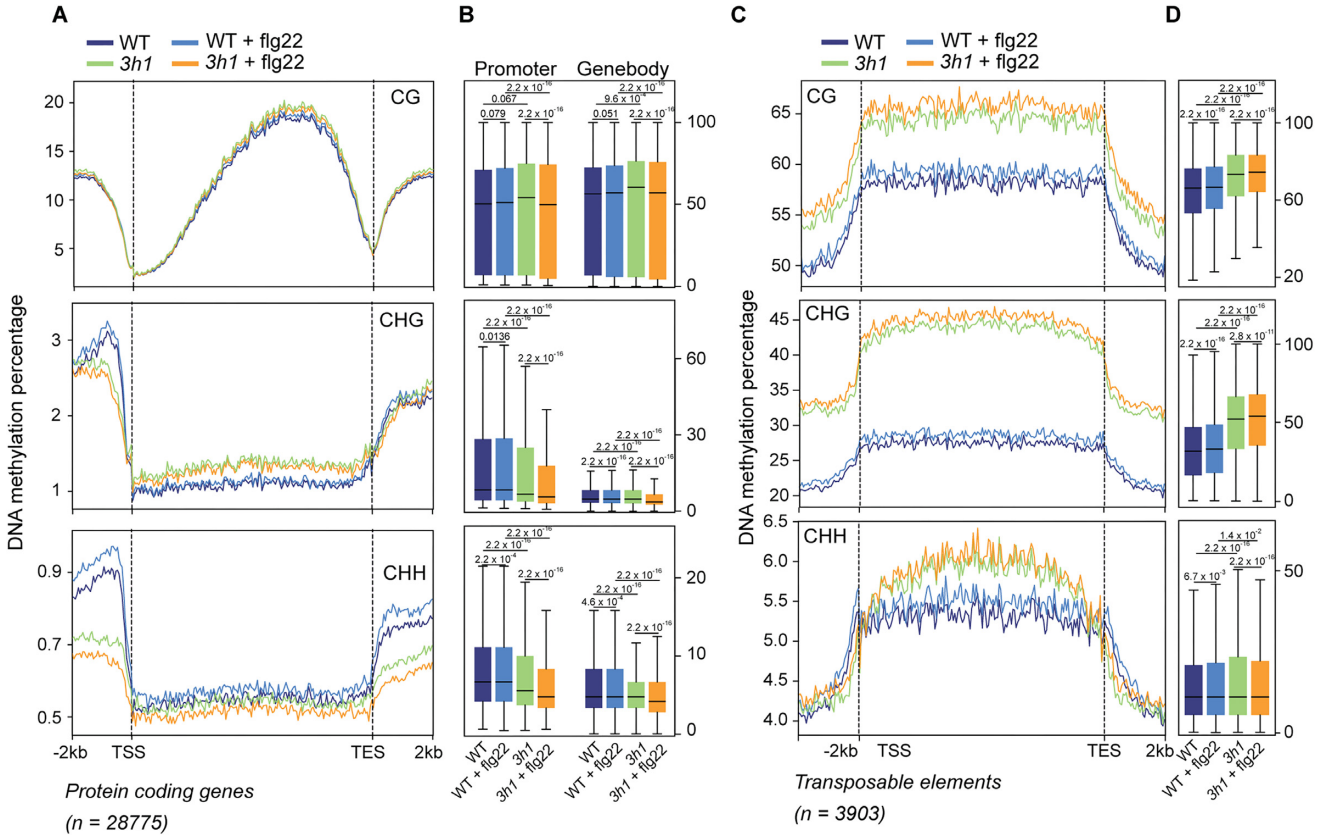

Figure 5. Global methylation profiles are altered in *3h1* plants and after flg22-treatment. (**A**) Distribution of DNA methylation in all three sequence contexts in WT, WT + flg22, *3h1* and *3h1* + flg22 over protein coding genes (PCGs). Biological replicates were combined as one sample. Independent biological replicates are shown in Supplementary Figure S6G–I. (**B**) Boxplots of all methylation percentages shown for promoter and gene body regions for the PCGs in all three contexts. (**C**, **D**) Average distribution and boxplots of WT, WT + flg22, *3h1* and *3h1* + flg22 from all three contexts in transposable elements (TEs).

increases at 6h of *Pst* DC3000 infection in flg22-treated WT plants but not in *3h1*. We observed that *3h1* plants exhibited an overall decrease in average promoter methylations of these genes in all contexts (Supplementary Figure S8). Interestingly, flg22 treatment increased the overall promoter methylation levels in *3h1* with no marked changes in WT (Supplementary Figure S8). Moreover, 44 genes from Cluster 1 directly involved in plant innate defense showed a striking anti-correlation between promoter CG, CHG and CHH methylation, respectively, and repressed expression patterns in *3h1* as compared to WT after flg22 treatment (Figure 6A–C). Interestingly, no significant promoter methylation changes were observed in WT for these genes after flg22 treatment while an opposite trend in all sequence contexts was obvious in *3h1* (Figure 6D–F). This further reiterates that H1 modulates flg22-induced DNA methylation dynamics and gene expression changes in plants. As flg22 enhanced PCG DNA methylation in all contexts (CG, CHH and CHG) in *3h1* mutant plants, we speculate that the altered gene expression of *WRKY29*, *PUB22 and Exo70H1* (Figure 4D and Supplementary Figure S4B) might be due to enhanced promoter DNA methylation at these gene loci. Accordingly, we observed increased methylation in flg22-treated *3h1* plants at these gene loci (Figure 6G–I).

H1 histones control H3K56ac levels in plants

H1 histones control the epigenetic landscape in animals by either promoting or inhibiting various H3 histone modifications (45). Since we also observed dynamic differential regulation of *HAC2* and *HDA18* in *3h1* and H1 and H3K56ac can act as antagonistic regulators of nucleosome dynamics (46), we speculated that H1 might also regulate the histone epigenetic profile. To this end, we tested the global levels of two well-known active and repressive marks H3K4me3, H3K27me3, respectively, as well as H3K56ac in flg22-primed and non-primed plants after *Pst* DC3000 infection. We observed no significant changes in H3K4me3 and H3K27me3 between *3h1* and WT plants (Supplementary Figure S9). In contrast, although H3K56ac levels were enhanced in *3h1* plants, we observed a dramatic decrease in H3K56ac levels in flg22-treated *3h1* mutant plants (Figure 7A). In contrast, flg22 treatment increased H3K56ac in WT plants, suggesting that H3K56ac is a crucial player in flg22-triggered priming in plants. Interestingly, the H3K56ac levels decreased upon *Pst* DC3000 infection, suggesting a possible strategy of the pathogen to overcome plant defense. The combined regulation of DNA methylation and histone modifications by H1 leads to a dynamic chromatin landscape (16). Finally, to test the state of chromatin compaction of some of the selected differentially regulated genes

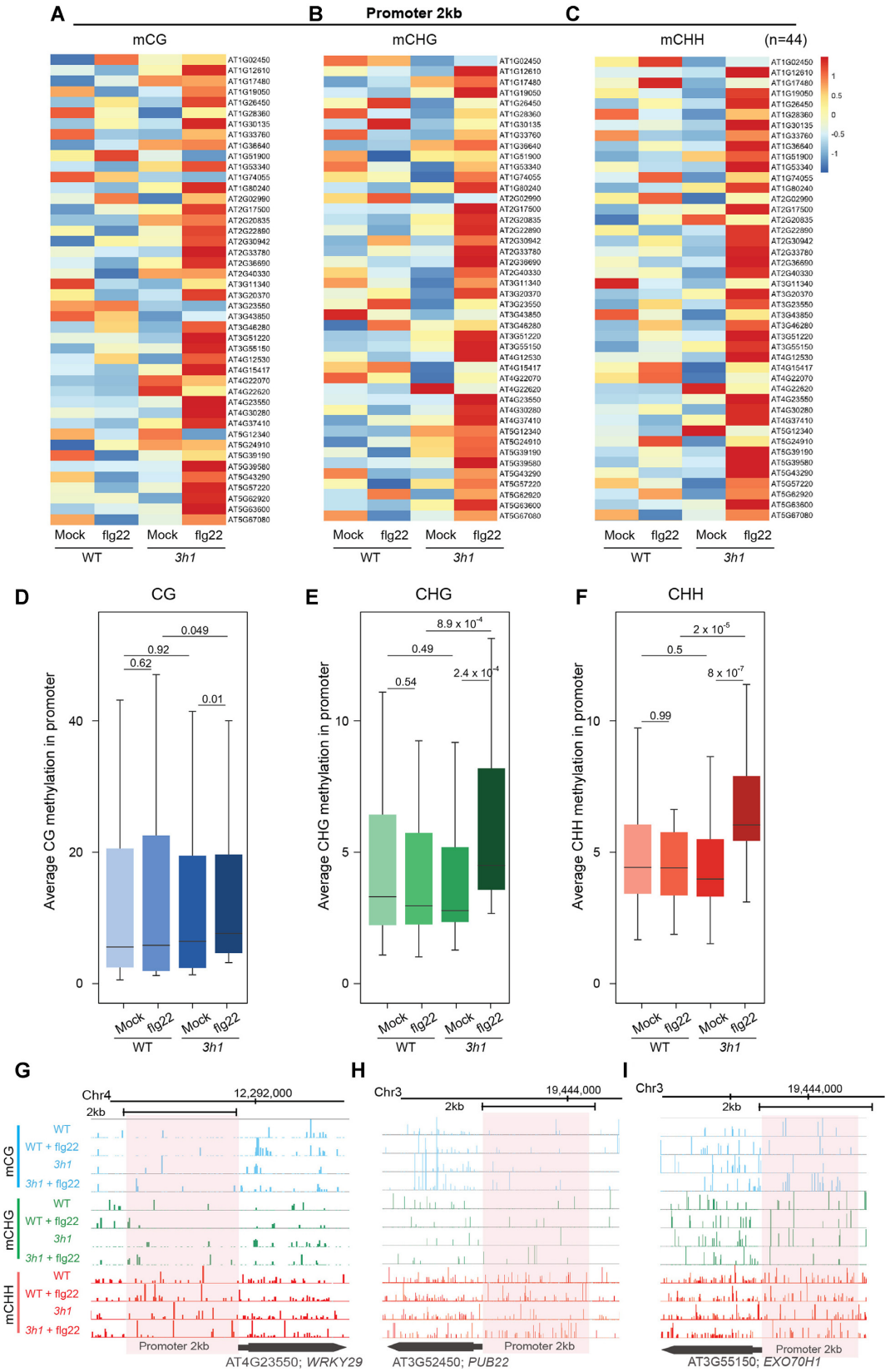

Figure 6. flg22 triggers differential methylation and gene expression in *3h1*. (**A–C**) Heatmap of mean promoter methylation in all contexts (CG, CHG and CHH) on selected transcripts from Cluster 1 (Figure 4D) in flg22-treated WT and *3h1* samples which showed differential expression after *Pst* DC3000 infection. (**D–F**) Boxplot of average methylations in indicated contexts in the promoter (–2 kb) of these genes. p value represents Wilcoxon test. (**G–I**) Genome Browser snapshots showing the distribution of CH, CHG and CHH methylation in representative defense genes *WRKY29*, *PUB22* and *Exo70H1*.

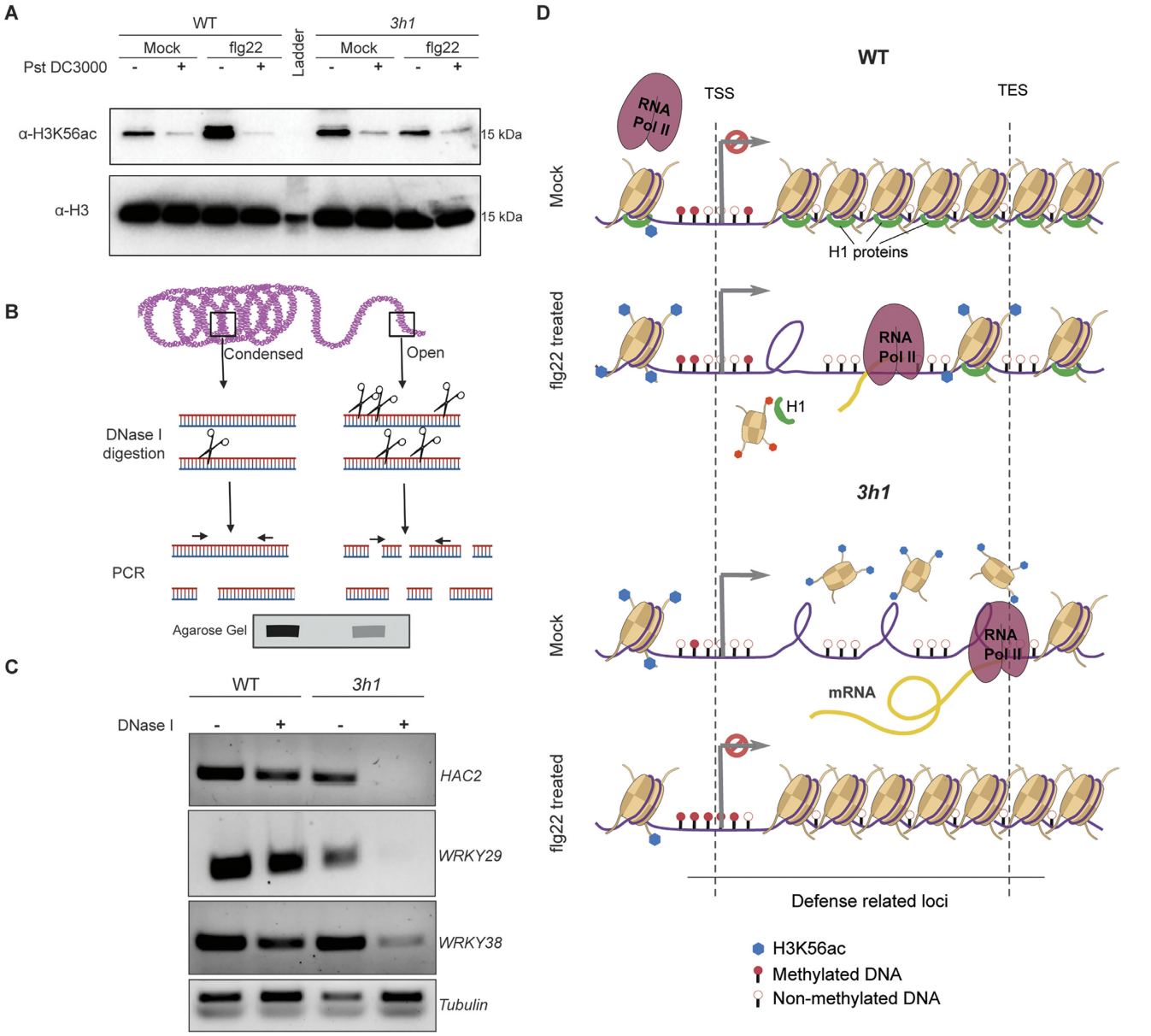

Figure 7. H1 controls H3K56ac levels in plants. (**A**) Western blot showing the H3K56ac levels in WT and *3h1* plants after water (mock) or flg22 treatment challenged with *Pst* DC3000 (6h). (**B**) Schematic representation showing the principle of the chromatin accessibility assay by DNase I digestion using PCR. Open chromatin is more frequently cut by limited DNase I digestion in small fragments giving reduced PCR signals while condensed chromatin which is less frequently cut gives strong PCR band signal. (**C**) DNase I accessibility PCR of *HAC2, WRKY29* and *WRKY38* in WT as compared to *3h1*. DNase I treatment was performed for 5 min at 37°C. (**D**) Model showing the dynamic changes in epigenetic landscape in *3h1* after flg22 treatment as compared to WT Arabidopsis plants.

in *3h1*, we performed DNase I accessibility assays (38) (Figure 7B). We observed that *WRKY29*, *HAC2* and *WRKY38* were more accessible to DNase I digestion in *3h1,* suggesting an open chromatin state for these genes (Figure 7C). However, the accessibility of *HDA18* and *WRKY62* was not significantly changed in *3h1,* reflecting a more complex regulation of chromatin accessibility (Supplementary Figure S10A). Conversely, the overall accessibility of *HAC2*, *WRKY29* and *WRKY38* to some extent was restricted by flg22 treatment in *3h1 (*Supplementary Figure S10B, C). Taken together, our data suggest that a multifaceted regulation of the chromatin landscape by H1 histones via dynamic DNA methylation and H3K56 acetylation mainly accounts for the defective priming phenotype in *3h1* plants (Figure 7D).

DISCUSSION

The role of linker histones is extensively studied in animal disease pathogenesis and progression (47). However, we lack an understanding of the role of H1 histones in plant immunity and disease. In this study, we aimed to understand the role of linker histone H1 in plant defense. The lack of developmental or pathogen phenotypes in single

mutants of Arabidopsis H1.1 and H1.2 reflects the redundancy of the linker histones (Figure 1). In contrast, animal studies showed that single H1 mutations lead to severe developmental defects or diseases (48). This can partly be explained by the cell type- and stage-specific isoforms present in animals, while three general isoforms of H1 exist in Arabidopsis (19). Accordingly, double *h1.1h1.2* and triple mutant *h1.1h1.2h.1.3* (*3h1*) plants show altered resistance to both bacterial and fungal pathogens. The developmental defects like stomatal spacing in *3h1* do not seem to influence the bacterial load in plants, as reflected by almost equal bacterial counts at 3 hpi (Figure 1B) (17). In *3h1,* the enhanced disease resistance is associated with enhanced PTI induction as reflected by elevated ROS and MAPK activation (Figure 2A, B). The enhanced PTI marker gene expression and elevated defense hormone SA levels further support the resistance phenotype of *3h1* mutant plants. The higher levels of phytoalexins like camalexin and callose in *3h1* mutant plants in control conditions (as also suggested by transcriptome analysis Cluster 6,7 and 9, Figure 3B) could also explain the resistant phenotype of *3h1* (Figure 1). Interestingly, after flg22 priming, WT plants show enhanced expression of defense-related genes like MAPKs and WRKYs compared to *3h1* (Cluster 1, Figure 4D) (43). The inability of flg22-treated *3h1* plants to mount a robust defense response after pathogen infection could lead to the observed non-priming phenotype (Figure 4A, B). This is also evident by the reduced camalexin and callose deposition in *3h1* after flg22 treatment (Supplementary Figure S3). The other major factors which correlate with the priming-deficient phenotype in *3h1* are the DNA methylation and histone acetylation changes in the mutant after flg22 treatment. The presence of H1 histones might present a physical barrier to DNA methyltransferases at PCG, which are activated by flg22 priming. De novo DNA methylation by the RNA-directed DNA methylation (RdDM) pathway as well as cross-talk between maintenance DNA methylation pathways might explain the increase in PCG methylation in all contexts in *3h1* after flg22 treatment (49). However, the drop in CHG and CHH but not in CG methylation at the promoters of genes in *3h1* mutant plants is in accordance with the redistribution of RdDM activity from euchromatic to heterochromatic regions in H1 mutants (23) (Figure 5). Likewise, the higher methylation of TEs in all contexts in *3h1* mutant plants is in agreement with the methylation patterns observed for long TEs in the double mutant *h1.1h1.2* (Figure 5) (21). The DNA methylation changes upon flg22 treatment in our study fit to the earlier reports of dynamic DNA methylation linked to differential gene expression in Arabidopsis after pathogen infection and PTI induction, although in our study flg22 treatment led to an overall increase of DNA methylation in WT, which was not described in previous reports (50,51). The effect of *Pst* DC3000 induced cell death could affect the overall DNA methylation levels in these studies; also the different time points, i.e. early time points of 3, 6 and 9 h for flg22 and late time point of 5d for SA treatment, could have different effects on the methylation landscape of the plants.

Linker H1 histones are normally associated with the compaction of chromatin and hinder the access of the transcription machinery to genes (12). This is also suggested by our data as we observe a higher number of differentially regulated genes in *3h1* under control conditions (Figure 5A). In the absence of H1, chromatin seems to be more accessible to enzymes for euchromatic histone modifications and antagonizes DNA methylation (21). For example, the histone acetyltransferase INCREASED DNA METHYLATION (IDM1) is important for preventing DNA hypermethylation, while the histone deacetylase HDA6 affects DNA methylation particularly in rDNA (52,53). We also observed that the histone acetyltransferase *HAC2* and the deacetylase *HDA18* were strongly upregulated in *3h1* mutant plants, which could promote chromatin decompaction, gene expression and influence DNA methylation (Figure 3D). This H1 dependent interplay between DNA methylation and histone modifiers prompted us to analyze the levels of histone marks in *3h1* before and after flg22 treatment. The higher levels of the H3K56ac activation mark in the absence of H1 (*3h1*) suggest the greater access of transcription factors to gene promoters (Figure 7A) (46). This makes sense as H3K56 is close to the exit-entry points of the nucleosomal DNA superhelix, which coincides with the position of linker histone H1. However, the minor changes observed in global H3K4me3 and H3K27me3 in *3h1* compared to WT indicate that H1 is not involved in these marks at the genome-wide scale, although local changes might be present, or changes were not observed due to the cell type-specific and developmental stage-specific nature of these modifications (54) (Supplementary Figure S9). Paradoxically, flg22 treatment downregulates *HAC2* and *HDA18* expression in *3h1* mutant plants, possibly leading to reduced histone H3K56ac levels, which may allow DNA methylation to target promoters of defense-related genes and lead to the observed hypermethylation after bacterial infection. The intricate crosstalk between DNA methylation and histone acetylation in *3h1* plants before and after flg22 treatment can lead to structurally more dynamic chromatin accessibility to the transcription machinery. Taken together, we provide evidence for the role of H1 in governing dynamic changes in DNA methylation and histone acetylation during plant immunity.

DATA AVAILABILITY

RNA seq and methylation data generated for this study have been deposited in the NCBI under accession number PRJNA814075. Additional data related to this paper may be requested from the authors.

SUPPLEMENTARY DATA

Supplementary Data are available at NAR Online.

ACKNOWLEDGEMENTS

We are grateful to Dr Kinga Rutowicz and Dr Célia Baroux from DPMB, University of Zurich, Switzerland for kindly sharing the H1 related mutant seeds and fruitful discussions. We are very thankful to Prof. Steve Jacobson and Colette Picard at UCLA for providing the pipeline for DNA methylation analysis. We also thank Lea Faivre and Daniel Schubert at FU Berlin and Moussa Benhamed at IPS, Paris for fruitful insights. We thank Dr. Mubashir Ahmad

from Ulm University for critically reading the manuscript. We also thank KAUST core lab for providing RNA seq and hormone quantification facilitates.

Author contributions: A.H.S. and H.H. conceptualized this study. A.H.S. performed most of the experiments. K.N., K.G. and M.G. analyzed RNA seq and Bisulfite seq data. NT performed some of the qPCR experiments. M.A.T. did phytohormone quantifications. H.A., M.A. and N.R. helped in performing initial patho-assays and data analysis. A.H.S., K.N., M.G. and H.H. wrote the manuscript. All authors read and approved the final manuscript.

FUNDING

King Abdullah University of Science and Technology (KAUST) [BAS/1/1062-01-01 to H.H.]. Funding for open access charge: King Abdullah University of Science and Technology (KAUST) [BAS/1/1062-01-01 to H.H.].

Conflict of interest statement. None declared.

REFERENCES

1. Jones,J.D.G. and Dangl,J.L. (2006) The plant immune system. *Nature*, **444**, 323–329.
2. Bigeard,J., Colcombet,J. and Hirt,H. (2015) Signaling mechanisms in pattern-triggered immunity (PTI). *Mol. Plant*, **8**, 521–539.
3. Berens,M.L., Berry,H.M., Mine,A., Argueso,C.T. and Tsuda,K. (2017) Evolution of hormone signaling networks in plant defense. *Annu. Rev. Phytopathol.*, **55**, 401–425.
4. Thomma,B.P.H.J., Nürnberger,T. and Joosten,M.H.A.J. (2011) Of PAMPs and effectors: the blurred PTI-ETI dichotomy. *Plant Cell*, **23**, 4–15.
5. Conrath,U., Beckers,G.J.M., Langenbach,C.J.G. and Jaskiewicz,M.R. (2015) Priming for enhanced defense. *Annu. Rev. Phytopathol.*, **53**, 97–119.
6. Chinchilla,D., Zipfel,C., Robatzek,S., Kemmerling,B., Nürnberger,T., Jones,J.D.G., Felix,G. and Boller,T. (2007) A flagellin-induced complex of the receptor FLS2 and BAK1 initiates plant defence. *Nature*, **448**, 497–500.
7. Gong,B.Q., Guo,J., Zhang,N., Yao,X., Wang,H.B. and Li,J.F. (2019) Cross-microbial protection via priming a conserved immune co-receptor through juxtamembrane phosphorylation in plants. *Cell Host Microbe*, **26**, 810–822.
8. Birkenbihl,R.P., Liu,S. and Somssich,I.E. (2017) Transcriptional events defining plant immune responses. *Curr. Opin. Plant Biol.*, **38**, 1–9.
9. Winkelmüller,T.M., Entila,F., Anver,S., Piasecka,A., Song,B., Dahms,E., Sakakibara,H., Gan,X., Kułak,K., Sawikowska,A. *et al.* (2021) Gene expression evolution in pattern-triggered immunity within Arabidopsis thaliana and across *Brassicaceae* species. *Plant Cell*, **33**, 1863–1887.
10. Kasinsky,H.E., Lewis,J.D., Dacks,J.B. and Ausló,J. (2001) Origin of H1 linker histones. *FASEB J.*, **15**, 34–42.
11. Zhou,B.R., Feng,H., Kato,H., Dai,L., Yang,Y., Zhou,Y. and Bai,Y. (2013) Structural insights into the histone H1-nucleosome complex. *Proc. Natl. Acad. Sci. U.S.A.*, **110**, 19390–19395.
12. Fyodorov,D.V., Zhou,B.-R., Skoultchi,A.I. and Bai,Y. (2018) Emerging roles of linker histones in regulating chromatin structure and function. *Nat. Rev. Mol. Cell Biol.*, **19**, 192–206.
13. Hergeth,S.P. and Schneider,R. (2015) The H1 linker histones: multifunctional proteins beyond the nucleosomal core particle. *EMBO Rep.*, **16**, 1439–1453.
14. Fan,Y., Nikitina,T., Zhao,J., Fleury,T.J., Bhattacharyya,R., Bouhassira,E.E., Stein,A., Woodcock,C.L. and Skoultchi,A.I. (2005) Histone H1 depletion in mammals alters global chromatin structure but causes specific changes in gene regulation. *Cell*, **123**, 1199–1212.
15. Rupp,R.A.W. and Becker,P.B. (2005) Gene regulation by histone H1: new links to DNA methylation. *Cell*, **123**, 1178–1179.
16. Yang,S.-M., Kim,B.J., Toro,L.N. and Skoultchi,A.I. (2013) H1 linker histone promotes epigenetic silencing by regulating both DNA methylation and histone H3 methylation. *Proc. Natl. Acad. Sci. U.S.A.*, **110**, 1708.
17. Rutowicz,K., Lirski,M., Mermaz,B., Teano,G., Schubert,J., Mestiri,I., Kroteń,M.A., Fabrice,T.N., Fritz,S., Grob,S. *et al.* (2019) Linker histones are fine-scale chromatin architects modulating developmental decisions in Arabidopsis. *Genome Biol.*, **20**, 157.
18. Shen,X., Yu,L., Weir,J.W. and Gorovsky,M.A. (1995) Linker histories are not essential and affect chromatin condensation in vivo. *Cell*, **82**, 47–56.
19. Kotliński,M., Knizewski,L., Muszewska,A., Rutowicz,K., Lirski,M., Schmidt,A., Baroux,C., Ginalski,K. and Jerzmanowski,A. (2017) Phylogeny-based systematization of Arabidopsis proteins with histone H1 globular domain. *Plant Physiol.*, **174**, 27–34.
20. Rutowicz,K., Puzio,M., Halibart-Puzio,J., Lirski,M., Kroteń,M.A., Kotliński,M., Kniżewski,Ł., Lange,B., Muszewska,A., Śniegowska-Świerk,K. *et al.* (2015) A specialized histone H1 variant is required for adaptive responses to complex abiotic stress and related DNA methylation in Arabidopsis. *Plant Physiol.*, **169**, 2080–2101.
21. Zemach,A., Kim,M.Y., Hsieh,P.H., Coleman-Derr,D., Eshed-Williams,L., Thao,K., Harmer,S.L. and Zilberman,D. (2013) The Arabidopsis nucleosome remodeler DDM1 allows DNA methyltransferases to access H1-containing heterochromatin. *Cell*, **153**, 193–205.
22. Rea,M., Zheng,W., Chen,M., Braud,C., Bhangu,D., Rognan,T.N. and Xiao,W. (2012) Histone H1 affects gene imprinting and DNA methylation in Arabidopsis. *Plant J.*, **71**, 776–786.
23. Choi,J., Lyons,D.B. and Zilberman,D. (2021) Histone H1 prevents non-CG methylation-mediated small RNA biogenesis in Arabidopsis heterochromatin. *Elife*, **10**, e72676.
24. Rayapuram,N., Jarad,M., Alhoraibi,H.M., Bigeard,J., Abulfaraj,A.A., Völz,R., Mariappan,K.G., Almeida-Trapp,M., Schlöffel,M., Lastrucci,E. *et al.* (2021) Chromatin phosphoproteomics unravels a function for AT-hook motif nuclear localized protein AHL13 in PAMP-triggered immunity. *Proc. Natl. Acad. Sci. U.S.A.*, **118**, e2004670118.
25. Ranf,S., Eschen-Lippold,L., Pecher,P., Lee,J. and Scheel,D. (2011) Interplay between calcium signalling and early signalling elements during defence responses to microbe- or damage-associated molecular patterns. *Plant J.*, **68**, 100–113.
26. Trapp,M.A., De Souza,G.D., Rodrigues-Filho,E., Boland,W. and Mithöfer,A. (2014) Validated method for phytohormone quantification in plants. *Front. Plant Sci.*, **5**, 417.
27. Wang,Y., Li,X., Fan,B., Zhu,C. and Chen,Z. (2021) Regulation and function of defense-related callose deposition in plants. *Int. J. Mol. Sci.*, **22**, 2393.
28. Bolger,A.M., Lohse,M. and Usadel,B. (2014) Trimmomatic: a flexible trimmer for Illumina sequence data. *Bioinformatics*, **30**, 2114–2120.
29. Kim,D., Pertea,G., Trapnell,C., Pimentel,H., Kelley,R. and Salzberg,S.L. (2013) TopHat2: accurate alignment of transcriptomes in the presence of insertions, deletions and gene fusions. *Genome Biol.*, **14**, R36.
30. Quinlan,A.R. and Hall,I.M. (2010) BEDTools: a flexible suite of utilities for comparing genomic features. *Bioinformatics*, **26**, 841–842.
31. Love,M.I., Huber,W. and Anders,S. (2014) Moderated estimation of fold change and dispersion for RNA-seq data with DESeq2. *Genome Biol.*, **15**, 550.
32. Tian,T., Liu,Y., Yan,H., You,Q., Yi,X., Du,Z., Xu,W. and Su,Z. (2017) agriGO v2.0: a GO analysis toolkit for the agricultural community, 2017 update. *Nucleic. Acids Res.*, **45**, W122–W129.
33. Cokus,S.J., Feng,S., Zhang,X., Chen,Z., Merriman,B., Haudenschild,C.D., Pradhan,S., Nelson,S.F., Pellegrini,M. and Jacobsen,S.E. (2008) Shotgun bisulphite sequencing of the Arabidopsis genome reveals DNA methylation patterning. *Nature*, **452**, 215–219.
34. Langmead,B. and Salzberg,S.L. (2012) Fast gapped-read alignment with Bowtie 2. *Nat. Methods*, **9**, 357.
35. Krueger,F. and Andrews,S.R. (2011) Bismark: a flexible aligner and methylation caller for Bisulfite-Seq applications. *Bioinformatics*, **27**, 1571–1572.
36. Ramírez,F., Dündar,F., Diehl,S., Grüning,B.A. and Manke,T. (2014) deepTools: a flexible platform for exploring deep-sequencing data. *Nucleic. Acids Res.*, **42**, W187.
37. Ramirez-Prado,J.S., Latrasse,D. and Benhamed,M. (2021) Histone modification ChIP-seq on *Arabidopsis thaliana* plantlets. *Bio-protocol*, **11**, e4211.

38. Shu,H., Gruissem,W. and Hennig,L. (2013) Measuring Arabidopsis chromatin accessibility using DNase I. Polymerase chain reaction and DNase I-chip assays. *Plant Physiol.*, **162**, 1794–1801.
39. Torres,M.A., Dangl,J.L. and Jones,J.D.G. (2002) Arabidopsis gp91phox homologues AtrbohD and AtrbohF are required for accumulation of reactive oxygen intermediates in the plant defense response. *Proc. Natl. Acad. Sci. U.S.A.*, **99**, 517–522.
40. Kim,K.C., Lai,Z., Fan,B. and Chen,Z. (2008) Arabidopsis WRKY38 and WRKY62 transcription factors interact with histone deacetylase 19 in basal defense. *Plant Cell*, **20**, 2357.
41. Piasecka,A., Jedrzejczak-Rey,N. and Bednarek,P. (2015) Secondary metabolites in plant innate immunity: conserved function of divergent chemicals. *New Phytol.*, **206**, 948–964.
42. Mauch-Mani,B., Baccelli,I., Luna,E. and Flors,V. (2017) Defense priming: an adaptive part of induced resistance. *Annu. Rev. Plant Biol.*, **68**, 485–512.
43. Asai,T., Tena,G., Plotnikova,J., Willmann,M.R., Chiu,W.L., Gomez-Gomez,L., Boller,T., Ausubel,F.M. and Sheen,J. (2002) MAP kinase signalling cascade in Arabidopsis innate immunity. *Nature*, **415**, 977–983.
44. Bourguet,P., Picard,C.L., Yelagandula,R., Pélissier,T., Lorković,Z.J., Feng,S., Pouch-Pélissier,M.N., Schmücker,A., Jacobsen,S.E., Berger,F. *et al.* (2021) The histone variant H2A.W and linker histone H1 co-regulate heterochromatin accessibility and DNA methylation. *Nat. Commun.*, **12**, 2683.
45. Willcockson,M.A., Healton,S.E., Weiss,C.N., Bartholdy,B.A., Botbol,Y., Mishra,L.N., Sidhwani,D.S., Wilson,T.J., Pinto,H.B., Maron,M.I. *et al.* (2020) H1 histones control the epigenetic landscape by local chromatin compaction. *Nature*, **589**, 293–298.
46. Bernier,M., Luo,Y., Nwokelo,K.C., Goodwin,M., Dreher,S.J., Zhang,P., Parthun,M.R., Fondufe-Mittendorf,Y., Ottesen,J.J. and Poirier,M.G. (2015) Linker histone H1 and H3K56 acetylation are antagonistic regulators of nucleosome dynamics. *Nat. Commun.*, **6**, 10152.
47. Ye,X., Feng,C., Gao,T., Mu,G., Zhu,W. and Yang,Y. (2017) Linker histone in diseases. *Int. J. Biol. Sci.*, **13**, 1008–1018.
48. Behrends,M. and Engmann,O. (2020) Linker histone H1.5 is an underestimated factor in differentiation and carcinogenesis. *Environ. Epigenetics*, **6**, dvaa013.
49. Du,J., Johnson,L.M., Jacobsen,S.E. and Patel,D.J. (2015) DNA methylation pathways and their crosstalk with histone methylation. *Nat. Rev. Mol. Cell Biol.*, **16**, 519–532.
50. Yu,A., Lepère,G., Jay,F., Wang,J., Bapaume,L., Wang,Y., Abraham,A.L., Penterman,J., Fischer,R.L., Voinnet,O. *et al.* (2013) Dynamics and biological relevance of DNA demethylation in Arabidopsis antibacterial defense. *Proc. Natl. Acad. Sci. U.S.A.*, **110**, 2389–2394.
51. Dowen,R.H., Pelizzola,M., Schmitz,R.J., Lister,R., Dowen,J.M., Nery,J.R., Dixon,J.E. and Ecker,J.R. (2012) Widespread dynamic DNA methylation in response to biotic stress. *Proc. Natl. Acad. Sci. U.S.A.*, **109**, E2183–E2191.
52. Qian,W., Miki,D., Zhang,H., Liu,Y., Zhang,X., Tang,K., Kan,Y., La,H., Li,X., Li,S. *et al.* (2012) A histone acetyltransferase regulates active DNA demethylation in Arabidopsis. *Science*, **336**, 1445–1448.
53. Probst,A.V., Fagard,M., Proux,F., Mourrain,P., Boutet,S., Earley,K., Lawrence,R.J., Pikaard,C.S., Murfett,J., Furner,I. *et al.* (2004) Arabidopsis histone deacetylase HDA6 is required for maintenance of transcriptional gene silencing and determines nuclear organization of rDNA repeats. *Plant Cell*, **16**, 1021–1034.
54. Geeven,G., Zhu,Y., Kim,B.J., Bartholdy,B.A., Yang,S.M., Macfarlan,T.S., Gifford,W.D., Pfaff,S.L., Verstegen,M.J.A.M., Pinto,H. *et al.* (2015) Local compartment changes and regulatory landscape alterations in histone H1-depleted cells. *Genome Biol.*, **16**, 289.